

# FLOW DIRECTIONS OF RIVERS ARE SET BY THE MANTLE

SUBMITTED, NON-PEER REVIEWED MANUSCRIPT, COMPILED JULY 21, 2020

Alex G. Lipp<sup>1\*</sup> and Gareth G. Roberts<sup>1</sup>

<sup>1</sup>Department of Earth Sciences and Engineering, Imperial College London, UK

## ABSTRACT

Large rivers play crucial roles in determining loci of civilisation, natural resources and biodiversity. The positions of their mouths control nutrient and sediment supply to oceans. The paths that rivers take across the Earth's surface varies considerably with scale. For example, at large scales big North American rivers (e.g. Mississippi, Colorado, Columbia) have simple flow paths that can be described by a few changes in direction. However, at smaller scales, in headwaters or meanders for example, their paths can change rapidly. We map the scales at which river planforms are set so that their positions can be compared to driving processes at appropriate scales (e.g. lithology, mantle convection, biota). To do so, we develop a spectral methodology to map azimuths as a function of distance and scale (wavenumber). The resultant maps of azimuth in distance-wavenumber space are compared to independent environmental variables (e.g. lithology, dynamic topography, crust and lithospheric thickness) across the scales of interest, here 1–10<sup>3</sup> km. The results show that the flow directions of large rivers in Western North America are set at large scales, O(10<sup>3</sup>) km, and follow patterns of mantle convection. Planforms of major rivers, and as a result loci of civilisation, natural resources and chemical efflux to the oceans, are therefore principally driven by evolution of the solid Earth.

## 1 INTRODUCTION

Despite its general importance the way in which drainage networks acquire their planforms is poorly understood across the scales of interest. Evolution of the solid Earth is an obvious means to determine flow paths via lithospheric motions driven by, for example, orogenesis and mantle convection. Geologic, hydraulic, sedimentological and biotic processes also control flow paths. Antecedence, hysteresis, complex erosional processes and human intervention are also important means by which drainage networks can be generated and transmogrified (Cox 1989; Rinaldo et al. 1993; Anderson et al. 2010). Processes controlling drainage planforms are scale dependent. Our contribution has two parts. First, it is concerned with deconvolving drainage planforms into constituent scales and, second, with comparing filtered planforms to environmental variables at appropriate locations and scales.

In many instances visual inspection of drainage planforms provides most of the information we need. For example, the Colorado river, which drains western North America, flows mostly to the west, southwest and south in its upper, mid- and lower reaches, respectively (Figure 1). The planform of rivers atop topographic swells in other continents also have similarly simple patterns at long, O(10<sup>3</sup>–10<sup>4</sup>) km, wavelengths (Rudge et al. 2015). At these long wavelengths rivers mostly flow away from crests of topographic swells that are supported by the mantle (Roberts et al. 2012; Braun et al. 2013; Faccenna et al. 2019). This pattern of emergent simplicity at long wavelengths is manifest in the flow paths of many large rivers draining topographic swells and tectonic topography on Earth (e.g. African swells, Colorado Plateau, Mexican Highlands, East Australian Highlands, Himalayas) and elsewhere (e.g. Tharsis Rise, Mars) (Black et al. 2017). However, most rivers clearly do not have simple flow paths at all lengths scales. At short (< 100 km) length scales they can be extremely variable, which sometimes results

in rivers flowing in the opposite direction to the long wavelength direction of flow (e.g. Goosenecks, San Juan river, North America). These simple observations indicate that river planforms are scale dependent. To formalise these observations we develop a spectral methodology to map planforms and flow directions as a function of scale and position. We use this approach to compare drainage patterns to environmental variables at appropriate scales.

## 2 DATA AND METHODS

Standard (e.g. Fourier) spectral analysis is generally not well suited to transforming non-stationary signals (e.g. rivers), instead we make use of continuous wavelet transforms (Daubechies 1990; Farge 1992; Kumar et al. 1997; Torrence et al. 1998). There is a precedent for transforming directional time series into the frequency and frequency-distance domains in the atmospheric and oceanic sciences and a spherical harmonic approach has been used to compare flow directions of rivers to long wavelength topography (Donelan et al. 1985, 1996; Black et al. 2017). Recent wavelet spectral analyses of longitudinal river profiles (i.e. elevation as a function of distance,  $z(x)$ ) has shown that the shape of large African rivers is mostly determined at wavelengths > 100 km where their power spectra,  $\phi(k)$ , can be characterised as red noise, i.e.  $\phi \propto k^{-2}$ , where  $k$  is wavenumber (Roberts 2019). At shorter wavelengths power appears to have a pink noise spectrum,  $\phi \propto k^{-1}$ . These observations give a basis for modelling longitudinal river profiles as systems that possess self-similar scaling and deterministic behaviour at long wavelengths that emerges through local complexity. It gives a basis for understanding why at large length scales, O(10<sup>2</sup>–10<sup>3</sup>) km, river profiles atop dynamically supported topography (e.g. Bié dome, West Africa) have common shapes (Roberts et al. 2019). In this study, we develop wavelet spectral techniques to map flow directions of continental-scale drainage patterns as

\*correspondence: a.lipp18@imperial.ac.uk,

gareth.roberts@imperial.ac.uk

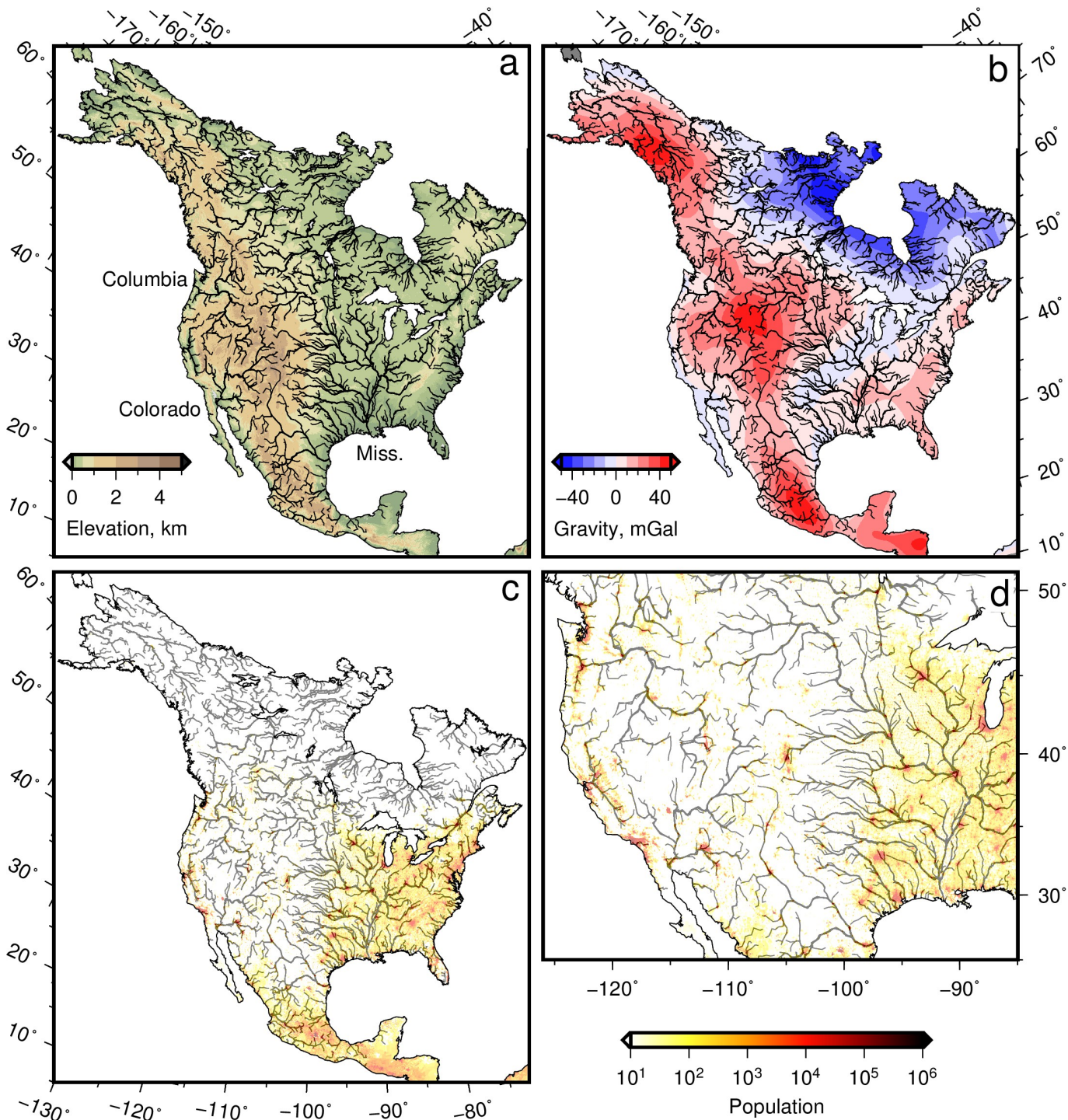


Figure 1: **North American drainage atop topography and long wavelength free-air gravity.** (a) Selected North American drainage networks extracted from ASTER DEM atop ETOPO1 DEM. Major rivers in this study are labeled; Miss = Mississippi. (b) Drainage atop long wavelength (> 800 km) GRACE free-air gravity anomalies; contour interval = 10 mGal (Tapley et al. 2005). If admittance  $Z \sim 25$  mGal/km, calculated dynamic support of western North America is up to  $\sim 1.5$  km. Note broadly radial drainage patterns that flow away from crests of positive dynamic topography (red contours). (c) and (d) Human population in 2015 from 2.5 minute GPW dataset. Note loci of highly populated areas (red blobs) and rivers.

a function of distance and wavelength. An important issue is that directional data contain discontinuities (e.g. at poles) so we transform the complex form of the time series (see Methods).

### 3 RESULTS AND DISCUSSION

Figure 2 shows the results of transforming the flow direction of the Colorado river into distance-wavenumber space. Figure 2a shows measured azimuths from an evenly resampled ( $\delta x = 2$  km) dataset alongside the filtered time series for wavelengths  $> 100$  km and  $> 1000$  km. Figure 2b shows Colorado river azimuths as a function of distance and wavelength ( $1/k$ ). In Figure 2c the azimuths for the full resolution dataset are shown as vectors with the observed river superimposed on top. These vectors are spread broadly uniformly between  $150^\circ \leq \theta \leq 300^\circ$  (see rose diagram aside Figure 2c). Note that the map has been rotated. The filtered  $> 100$  km and  $> 1000$  km azimuths and their associated rose diagrams are shown in Figures 2d and 2e. These long wavelength flow directions have, as expected, a smaller spread than the full dataset. The long wavelength azimuthal time series ( $\lambda > 1000$  km) quantifies flow paths mapped by eye in the introductory section, i.e. flow to west ( $\sim 270^\circ$ ), southwest ( $\sim 240^\circ$ ) and south ( $\sim 190^\circ$ ) in the upper, mid and lower reaches of the river, respectively (Figure 2f).

The white curve in Figure 2f shows a pseudo-Colorado river path generated using only azimuths at wavelengths  $> 1000$  km and forward geodetic transformation. This calculated flow path reinforces our assertion that most of the long wavelength structure of the Colorado river is set by just two changes in flow direction. Transformation of other major rivers and their tributaries reveal similarly simple flow paths (e.g. Mississippi, Columbia, Colorado; Figures 3a & 3b).

Gravity anomalies, tomographic models, magmatism and isostatic calculations indicate that western North American topography is principally a consequence of sub-crustal support moderated by tectonic and erosional processes (Atwater 1970; Wernicke 1985; Fernandes et al. 2019). A guide to the amplitude and wavelength of sub-plate support is the transfer function (admittance) between long wavelength free-air gravity and topography (McKenzie 2010). We note that gravity anomalies at spherical harmonic degrees appropriate for this study are particularly sensitive to upper mantle structure (Colli et al. 2016). In western North America the calculated admittance is  $\sim 25 \pm 3$  mGal/km at wavelengths  $> 1000$  km, which implies that up to  $\sim 1.5$  km of western North American topography is supported by the mantle (Stephenson et al. 2014). Figure 3b shows long wavelength free-air gravity from the GRACE dataset filtered to extract wavelengths between  $\sim 800$ – $2500$  km (Tapley et al. 2005). We have plotted the long wavelength azimuths of major rivers draining western North America atop these gravity anomalies in Figure 3b, which shows a strikingly radial pattern of flow directions away from the crest of predicted sub-plate support.

The black vectors in Figure 3c and 3d show mean flow directions of the first 500 km of major rivers draining the Colorado-Rocky-Mountains plateaux filtered to remove wavelengths  $< 1000$  km. In all cases flow is directed away from the crest of topography centred on Yellowstone and the Rio Grande rift. Figures 3e shows, for the same region, shear-wave velocity at 75 km depth from a recent tomographic model that incorporates data from

the USArray experiment (Shen et al. 2016). Lithospheric thicknesses generated by converting a global shear wave tomographic model into temperature using an empirical parameterisation are shown in Figure 3f (Ho et al. 2016). Cenozoic magmatism from the NAVDAT database and surficial geology from the GMNA repository are shown in Figures 3g and 3h. Furthermore, there is no obvious correlation between most long wavelength azimuths and surficial geology or crustal thicknesses (Buehler et al. 2017). An exception is that westernmost Cenozoic magmatism tends to be concentrated atop the crest of the swell (e.g. Figure 3g & 3h). All of the analysed drainage networks show long wavelength flow directed away from regions of low shear-wave velocity, positive gravity anomalies and embayments of thin lithosphere. These observations, combined with admittance between gravity and topography, are strongly suggestive of topography and drainage patterns maintained by mantle convection.

Finally, we examine ways in which observed planform distributions can be generated by forcing a landscape evolution model with calculated sub-plate support. A similar problem has been examined by parameterising landscape evolution models using uplift predicted from ‘backwards in time’ global convection models (Braun et al. 2013; Faccenna et al. 2019). Such simulations have shown that timescales of drainage planform evolution can depend on histories of sub-plate support. Additionally, inversion of drainage patterns has shown that continental-scale uplift histories can be determined that honour spot measurements of uplifted marine rock and to some extent thermochronometric and sedimentary flux observations (e.g. Rudge et al. 2015). Such results have been used to parameterise landscape evolution simulations for North America which yield broadly stable Cenozoic drainage planforms (Fernandes et al. 2019). These results give a basis for developing a very simple landscape evolution model in which initial conditions are generated using a simple uplift history, a small amount of uniform noise and fixed (Dirichlet;  $z = 0$ ) boundary conditions at the margins of the model domain. The initial condition is generated from dynamic topography calculated by converting long wavelength free-air gravity anomalies using an admittance of 25 mGal/km (Figure 1b). We note that this surface is similar to cumulative post-Cretaceous uplift mapped using the distribution of marine rocks in western North America, and its crest coincides with loci of Cenozoic basaltic magmatism (Klocking et al. 2018; Fernandes et al. 2019). The resultant surface is subsequently eroded for 5 ka using the well known stream power formulation of fluvial erosion, which has the form of a non-linear advective equation

$$\frac{\partial z}{\partial t} = -vA^m \nabla z, \quad (1)$$

where  $z$  is elevation,  $t$  is time, and  $A$  is upstream drainage area (Howard et al. 1983; Rosenbloom et al. 1994; Tinkler et al. 1998; Whipple et al. 1999). Erosional constants  $v = 3.62 \text{ m}^{0.3} / \text{Ma}$  and  $m = 0.35$  were calibrated for North America using incision measurements in the Grand Canyon (Fernandes et al. 2019). Prior to solving Equation 1 topographic sinks were filled, it was then solved numerically using the LandLab package (Barnes et al. 2014; Hobbey et al. 2017).

Figure 4 shows calculated topography and drainage areas. This simple model does not include the coastline, nor transcurrent, extensional or compressional plate motions or complex hydraulic

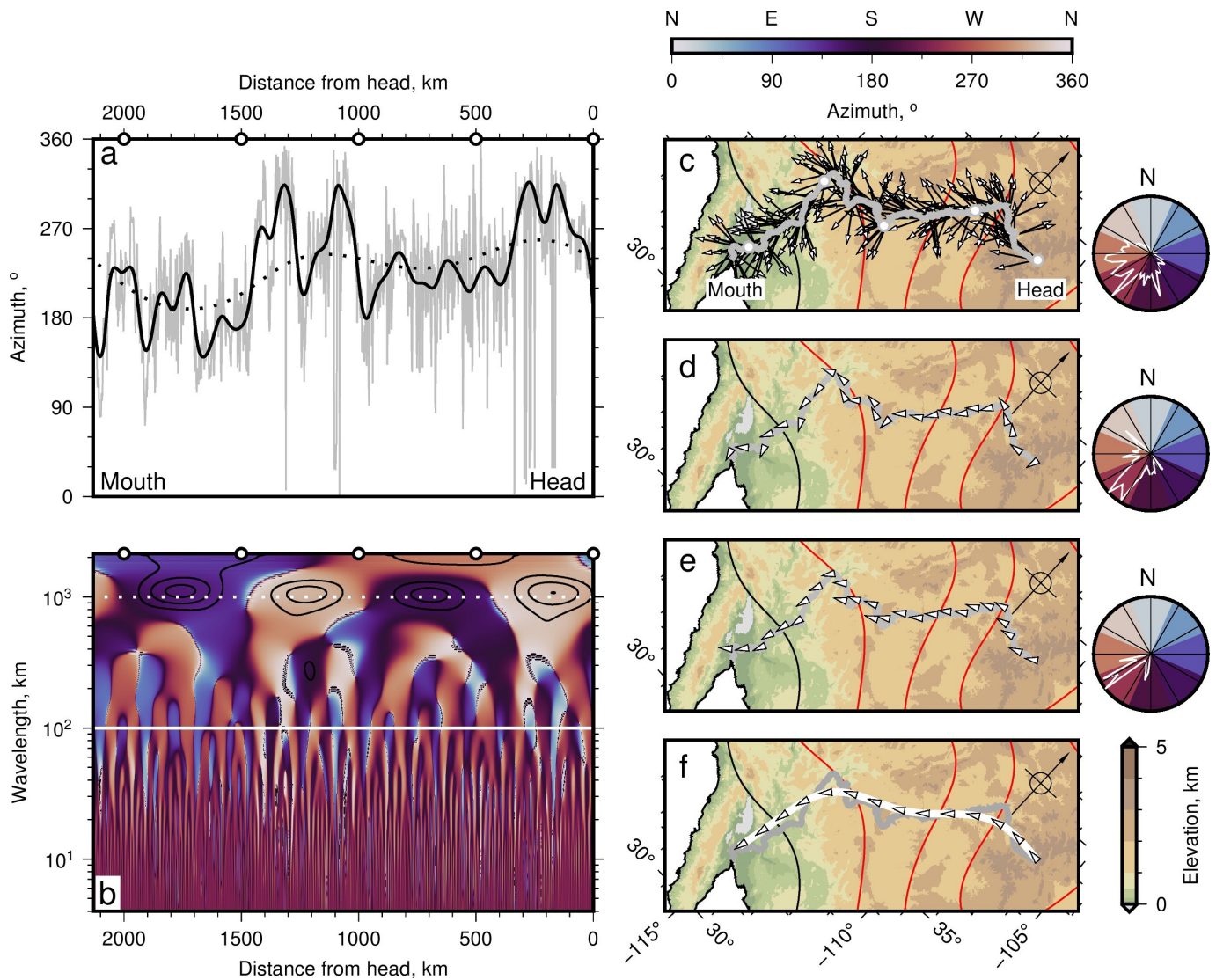
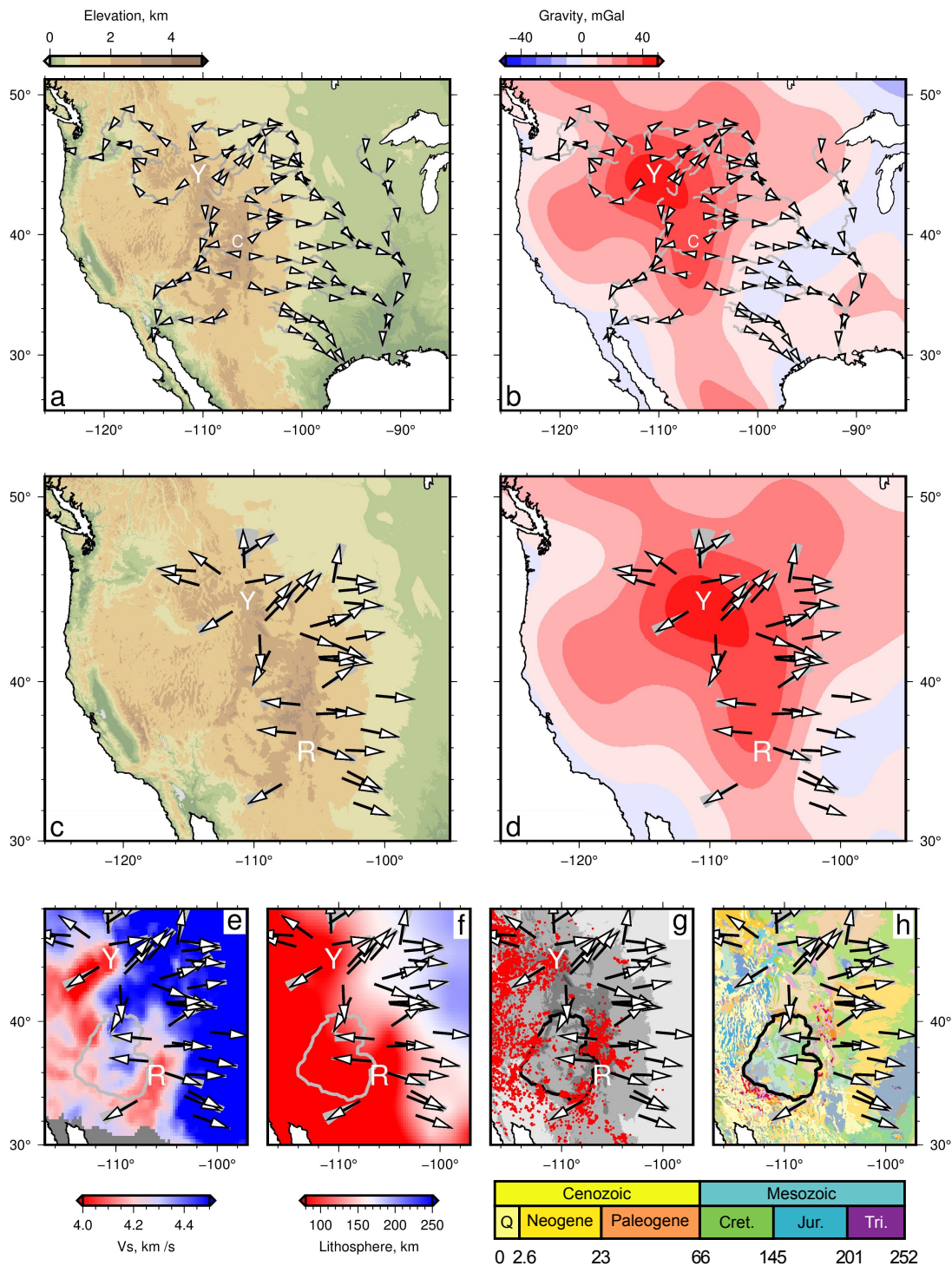


Figure 2: **Deconvolution of flow directions: Example from Colorado river.** (a) Gray curve = calculated azimuths of Colorado river ( $\delta x = 2$  km). Solid and dotted black curves = azimuths filtered to remove wavelengths  $\lambda < 100$  km and  $< 1000$  km, respectively. Note that distance is from river head and azimuths are measured in downstream direction. (b) Azimuths as function of distance and wavelength. Colours are centred on cardinals and intercardinals; light blue/dark blue/purple/orange = north/east/south/west; see scale bar and rose diagrams aside panels c–e. Solid and dotted white lines = 1000 km and 100 km wavelengths, respectively. Black contours = regions with highest power. White circles atop panel = positions along river (see panel c). (c) Colorado river (gray) and flow directions (azimuths) of full resolution dataset ( $\delta x = 2$  km); directions are shown every  $\sim 10$  km for clarity. White circles = distances shown atop panels (a) and (b). Colours/contours = topography/long wavelength ( $> 800$  km) free-air gravity anomalies, contour interval = 10 mGal, red/black contours = positive/zero values. Inset compass rose points north. Rose diagram aside shows azimuths of full resolution dataset ( $\delta x = 2$  km) in  $5^\circ$  bins (white polygon); rose sectors are coloured by azimuth (see panel b). (d) & (e) White vectors = azimuths calculated using wavelengths  $\lambda > 100$  km and  $> 1000$  km, respectively. Gray = Colorado river. Rose diagrams aside show calculated azimuths for filtered datasets in  $5^\circ$  bins. (f) White curve = river planform from geodetic transform of long wavelength azimuths. Vectors = long wavelength ( $> 1000$  km) flow azimuths shown every  $\sim 150$  km for clarity.



**Figure 3: Planform deconvolution.** (a) Flow directions (white vectors) atop major tributaries of the Colorado, Columbia and Mississippi rivers (gray curves). Vectors were generated from transformed river azimuths filtered to remove wavelengths < 1000 km and are shown every ~ 300 km for clarity, nearby parts of these rivers have similar azimuths. Y = Yellowstone; C = Colorado river shown in Figure 2. (b) Rivers and long wavelength azimuths atop long wavelength free-air gravity anomalies (Figure 1). (c) & (d) Black/gray vectors = average/all long wavelength (> 1000 km) azimuths for first 500 km of major rivers shown in panels (a) and (b). R = Rio Grande rift. Note rivers flow away from the crest of the western North American swell in a simple, broadly radial, pattern. (e) Flow paths atop USA.2016 shear wave tomographic model at 75 km depth (Shen et al. 2016). Gray polygon fringes Colorado Plateau. Y/R = Yellowstone/Rio Grande rift. (f) Flow atop CAM2016 lithospheric thickness map, which was generated by converting shear wave velocities into temperature (Ho et al. 2016). (g) Flow atop topography and Cenozoic magmatism (red circles) from NAVDAT inventory. (h) Flow atop surficial geology (GMNA dataset). Legend shows lithologies coloured by age; numbers = age in millions of years.

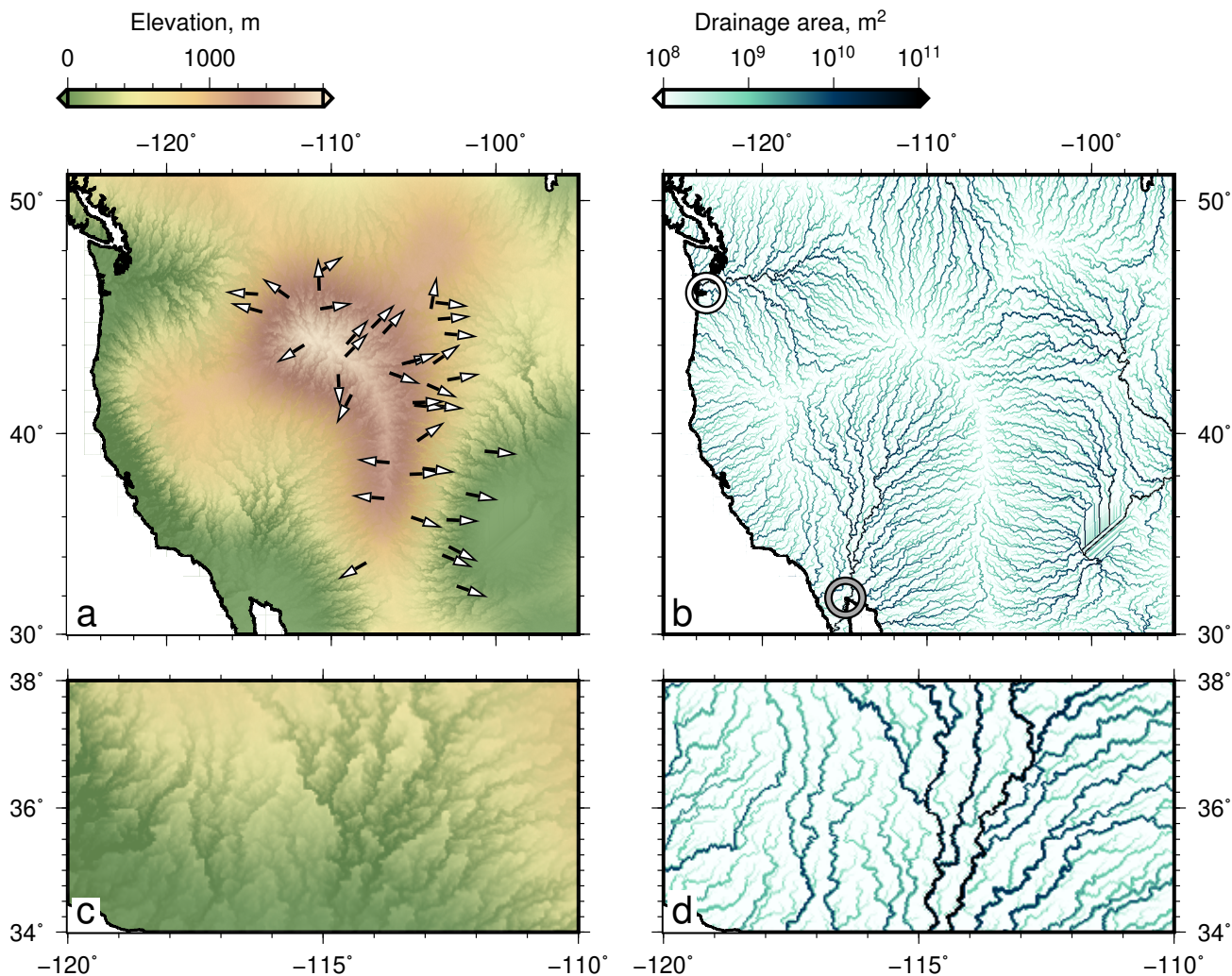


Figure 4: **Synthetic drainage patterns.** (a) Synthetic topography generated by solving the stream power erosional model using Landlab routines and an initial condition that includes calculated dynamic support and small amplitude (up to  $\pm 50$  m) random uniform noise. Coastline is shown but not used in this landscape simulation. Note radial drainage pattern away from swell crest; vectors show long wavelength azimuths of upper 500 km of actual rivers (see Figure 3b). (b) Predicted upstream drainage area, which is highest in channels. Mouths of actual Columbia/Colorado rivers are shown by white/gray circles. (c) Southern portion of topographic swell. (d) Drainage patterns along the southern portion of the swell. Note sinuous channels at small scale ( $< 100$  km) and radial pattern at larger scales.

or geomorphic processes (e.g. thresholds). Despite the simple formulation, the calculated positions of major rivers are essentially in the same locations as actual large rivers (e.g. Colorado, Columbia, Mississippi). We ran a suite of models in which the coastline and different distributions of noise between  $\pm 50$  m were inserted, which did not affect our principal conclusions. The positions of rivers at small scales is dependent on the distribution of noise (see Supplementary Material). We interpret these results as a strong indication that planforms of large western North American rivers are controlled principally by the mantle. Large scale planforms are moderated at smaller scales, O(1–10) km, by other environmental variables (e.g. lithology, biota, hydrodynamics).

#### 4 CONCLUSIONS

In this study a continuous wavelet approach is used to transform the complex form of distance-azimuth time series into the distance-wavenumber domain. We show how positions of the largest rivers in southern North America (Mississippi, Colorado, Columbia) are principally controlled by the shape of long wavelength O( $10^2$ – $10^3$ ) km topography. Seismic tomographic models, long wavelength free air gravity anomalies and the distribution of Cenozoic magmatism show that this topography was generated and is maintained by the mantle. A corollary is that the internal dynamics of the solid Earth play a crucial role in determining biodiversity, crucibles of civilisation and the distribution of natural resources.

#### CODE AVAILABILITY

Code for performing directional wavelet transforms can be downloaded from <https://github.com/alexlipp>. Wavelet transforms were performed using a modified version of the python mply library (Albanese et al. 2012; <http://mply.sourceforge.net>).

ASTER data can be accessed via <https://asterweb.jpl.nasa.gov/gdem.asp>, NAVDAT data: [www.navdat.org](http://www.navdat.org), geological maps: <https://ngmdb.usgs.gov/gmna>, tomographic models: <http://ds.iris.edu> and population data: <https://sedac.ciesin.columbia.edu>.

#### ACKNOWLEDGEMENTS

We thank F. Richards and V. Fernandes for helpful discussion. AGL is funded by NERC grant XYZ. This work was supported by CASP.

#### REFERENCES

- Albanese, D., R. Visintainer, S. Merler, S. Riccadonna, G. Jurman, and C. Furlanello (2012). *mly*: Machine Learning Python. arXiv: [1202.6548 \[cs\]](https://arxiv.org/abs/1202.6548).
- Anderson, R. S. and S. P. Anderson (2010). *Geomorphology: The Mechanics and Chemistry of Landscapes*. 1st ed. Cambridge, UK: Cambridge University Press.
- Atwater, T. (1970). “Implications of Plate Tectonics for the Cenozoic Tectonic Evolution of Western North America”. *Geological Society of America Bulletin* 81, pp. 3513–3536.
- Barnes, R., C. Lehman, and D. Mulla (2014). “Priority-flood: An optimal depression-filling and watershed-labeling algorithm for digital elevation models”. *Computers & Geosciences* 62, pp. 117–127. doi: [10.1016/j.cageo.2013.04.024](https://doi.org/10.1016/j.cageo.2013.04.024).
- Black, B. A., J. T. Perron, D. Hemingway, E. Bailey, F. Nimmo, and H. Zebker (2017). “Global drainage patterns and the origins of topographic relief on Earth, Mars, and Titan”. *Science* 356.6339, pp. 727–731. doi: [10.1126/science.aag0171](https://doi.org/10.1126/science.aag0171).
- Braun, J., X. Robert, and T. Simon-Labric (2013). “Eroding dynamic topography”. *Geophysical Research Letters* 40.8, pp. 1494–1499. doi: [10.1002/grl.50310](https://doi.org/10.1002/grl.50310).
- Buehler, J. S. and P. M. Shearer (2017). “Uppermost mantle seismic velocity structure beneath USArray”. *Journal of Geophysical Research: Solid Earth* 122.1, pp. 436–448. doi: [10.1002/2016JB013265](https://doi.org/10.1002/2016JB013265).
- Colli, L., S. Ghelichkhanand, and H.-P. Bunge (2016). “On the ratio of dynamic topography and gravity anomalies in a dynamic Earth”. *Geophysical Research Letters* 43, pp. 2510–2516. doi: [10.1002/2016GL067929](https://doi.org/10.1002/2016GL067929).
- Cox, K. G. (1989). “The role of mantle plumes in the development of continental drainage patterns”. *Nature* 342, pp. 873–877.
- Daubechies, I. (1990). “The wavelet transform, time-frequency localization and signal analysis”. *IEEE Transactions on Information Theory* 36.5, pp. 961–1005. doi: [10.1109/18.57199](https://doi.org/10.1109/18.57199).
- Donelan, M. A., W. M. Drennan, and A. K. Magnusson (1996). “Nonstationary Analysis of the Directional Properties of Propagating Waves”. *Journal of Physical Oceanography* 26.9, pp. 1901–1914. doi: [10.1175/1520-0485\(1996\)026<1901:NAOTDP>2.0.CO;2](https://doi.org/10.1175/1520-0485(1996)026<1901:NAOTDP>2.0.CO;2).
- Donelan, M. A., J. Hamilton, and W. H. Hui (1985). “Directional spectra of wind-generated ocean waves”. *Philosophical Transactions of the Royal Society of London. Series A, Mathematical and Physical Sciences* 315, pp. 509–562. doi: [10.1098/rsta.1985.0054](https://doi.org/10.1098/rsta.1985.0054).
- Faccenna, C., P. Glisovic, A. Forte, T. W. Becker, E. Garzanti, A. Sembroni, and Z. Gvirtzman (2019). “Role of dynamic topography in sustaining the Nile River over 30 million years”. *Nature Geoscience*. doi: [10.1038/s41561-019-0472-x](https://doi.org/10.1038/s41561-019-0472-x).
- Farge, M. (1992). “Wavelet transforms and their applications to turbulence”. *Annual Review of Fluid Mechanics* 24.1, pp. 395–458. doi: [10.1146/annurev.fl.24.010192.002143](https://doi.org/10.1146/annurev.fl.24.010192.002143).
- Fernandes, V. M., G. G. Roberts, N. White, and A. C. Whittaker (2019). “Continental-Scale Landscape Evolution: A History of North American Topography”. *Journal of Geophysical Research: Earth Surface* 124. doi: [10.1029/2018JF004979](https://doi.org/10.1029/2018JF004979).
- Ho, T., K. Priestley, and E. Debayle (2016). “A global horizontal shear velocity model of the upper mantle from multimode Love wave measurements”. *Geophysical Journal International* 207.1, pp. 542–561. doi: [10.1093/gji/ggw292](https://doi.org/10.1093/gji/ggw292).
- Hobley, D. E. J., J. M. Adams, S. S. Nudurupati, E. W. H. Hutton, N. M. Gasparini, E. Istanbuluoglu, and G. E. Tucker (2017). “Creative computing with Landlab: an open-source toolkit for building, coupling, and exploring two-dimensional numerical models of Earth-surface dynamics”. *Earth Surface Dynamics* 5.1, pp. 21–46. doi: [10.5194/esurf-5-21-2017](https://doi.org/10.5194/esurf-5-21-2017).
- Howard, A. D. and G. Kerby (1983). “Channel changes in badlands”. *GSA Bulletin* 94.6, pp. 739–752. doi: [10.1130/0016-7606\(1983\)94<739:CCIB>2.0.CO;2](https://doi.org/10.1130/0016-7606(1983)94<739:CCIB>2.0.CO;2).
- Klocking, M., N. J. White, J. MacLennan, D. McKenzie, and J. G. Fitton (2018). “Quantitative Relationships Between Basalt Geochemistry, Shear Wave Velocity, and Asthenospheric Temperature Beneath Western North America”. *Geochemistry, Geophysics, Geosystems* 19.9, pp. 3376–3404. doi: [10.1029/2018GC007559](https://doi.org/10.1029/2018GC007559).

- Kumar, P. and E. Foufoula-Georgiou (1997). “Wavelet analysis for geophysical applications”. *Reviews of Geophysics* 35.4, pp. 385–412. doi: [10.1029/97RG00427](https://doi.org/10.1029/97RG00427).
- McKenzie, D. (2010). “The influence of dynamically supported topography on estimates of  $T_e$ ”. *Earth and Planetary Science Letters* 295, pp. 127–138.
- Rinaldo, A., I. Rodriguez-Iturbe, R. Rigon, E. Ijjasz-Vasquez, and R. L. Bras (1993). “Self-organized fractal river networks”. *Phys. Rev. Lett.* 70 (6), pp. 822–825. doi: [10.1103/PhysRevLett.70.822](https://doi.org/10.1103/PhysRevLett.70.822).
- Roberts, G. G. (2019). “Scales of Similarity and Disparity Between Drainage Networks”. *Geophysical Research Letters* 46.7, pp. 3781–3790. doi: [10.1029/2019GL082446](https://doi.org/10.1029/2019GL082446).
- Roberts, G. G., N. J. White, G. L. Martin-Brandis, and A. G. Crosby (2012). “An uplift history of the Colorado Plateau and its surroundings from inverse modeling of longitudinal river profiles”. *Tectonics* 31.4. doi: [10.1029/2012TC003107](https://doi.org/10.1029/2012TC003107).
- Roberts, G. G., N. White, and B. H. Lodhia (2019). “The generation and scaling of longitudinal river profiles”. *Journal of Geophysical Research: Earth Surface* 124, pp. 137–153. doi: [10.1029/2018JF004796](https://doi.org/10.1029/2018JF004796).
- Rosenbloom, N. A. and R. S. Anderson (1994). “Hillslope and channel evolution in a marine terraced landscape, Santa Cruz, California”. *Journal of Geophysical Research: Solid Earth* 99.B7, pp. 14013–14029. doi: [10.1029/94JB00048](https://doi.org/10.1029/94JB00048).
- Rudge, J. F., G. G. Roberts, N. J. White, and C. N. Richardson (2015). “Uplift histories of Africa and Australia from linear inverse modeling of drainage inventories”. *Journal of Geophysical Research: Earth Surface* 120, pp. 894–914. doi: [10.1002/2014JF003297](https://doi.org/10.1002/2014JF003297).
- Shen, W. and M. H. Ritzwoller (2016). “Crustal and uppermost mantle structure beneath the United States”. *Journal of Geophysical Research: Solid Earth* 121.6, pp. 4306–4342. doi: [10.1002/2016JB012887](https://doi.org/10.1002/2016JB012887).
- Stephenson, S. N., G. G. Roberts, M. J. Hoggard, and A. C. Whittaker (2014). “A Cenozoic uplift history of Mexico and its surroundings from longitudinal river profiles”. *Geochemistry, Geophysics, Geosystems* 15, pp. 4734–4758. doi: [10.1002/2014GC005425](https://doi.org/10.1002/2014GC005425).
- Tapley, B., J. Ries, S. Bettadpur, D. Chambers, M. Cheng, F. Condi, B. Gunter, Z. Kang, P. Nagel, R. Pastor, T. Pekker, S. Poole, and F. Wang (2005). “GGM02 — An improved Earth gravity field model from GRACE”. *J. Geodesy* 79.467. doi: [10.1007/s00190-005-0480-z](https://doi.org/10.1007/s00190-005-0480-z).
- Tinkler, K. J. and E. E. Wohl (1998). *Rivers Over Rock: Fluvial Process in Bedrock Channels*. Washington, DC, USA: American Geophysical Union, Geophysical Monograph 107.
- Torrence, C. and G. P. Compo (1998). “A Practical Guide to Wavelet Analysis”. *Bulletin of the American Meteorological Society* 79, pp. 61–78.
- Wernicke, B. (1985). “Uniform-sense normal simple shear of the continental lithosphere”. *Canadian Journal of Earth Sciences* 22.1, pp. 108–125. doi: [10.1139/e85-009](https://doi.org/10.1139/e85-009).
- Whipple, K. X. and G. E. Tucker (1999). “Dynamics of the stream-power river incision model: Implications for height limits of mountain ranges, landscape response timescales, and research needs”. *Journal of Geophysical Research: Solid Earth* 104.B8, pp. 17661–17674. doi: [10.1029/1999JB900120](https://doi.org/10.1029/1999JB900120).

## SUPPORTING INFORMATION

This supplementary information contains, first, a description of data used to extract drainage patterns, second, methodologies to perform wavelet transformations of azimuthal time series, third, a discussion of uncertainties, and finally examples of synthetic landscape generated using different initial conditions to those shown in the main manuscript. Software to perform directional wavelet analysis: <https://github.com/alexlipp/directional-wavelets>.

*Data and Methods*

Transforming azimuth ‘time’ series has several simple steps. First, the drainage dataset is extracted from the ASTER GDEM, which has a horizontal resolution of  $\sim 30$  m, using Esri’s D8 (steepest descent) flow routing algorithms. Second, latitudes and longitudes are resampled along flow paths (e.g. rivers) so that they have equidistant spacing, which makes them straightforward to transform into the spectral domain. In the examples used in this paper  $\delta x = 2$  km. Third, distances and azimuths are calculated along the path. Local (point-to-point) azimuths,  $\theta(x)$ , are extracted using the `gmt mapproject` algorithm (see digital repository). Note that input is expected to be positions along a river with longitudes and latitudes in decimal degrees and resolution of up to a few tens of meters.

Applying wavelet transforms to azimuthal time series is generally problematical because the functions are not usually continuous —at least one pole contains a discontinuity, e.g.  $\sin(2\pi) = \sin(0)$ . To avoid this issue we transform the complex form of azimuthal time series,  $a(x)$ . Bearings can be considered as complex numbers of unit magnitude and variable phase,  $\theta$ . Making use of Euler’s formula any bearing,  $\theta$ , can be represented as  $\exp(i\theta)$  with real part  $\cos(\theta)$  and imaginary part  $\sin(\theta)$ , which correspond to northings and eastings, respectively. The complex time series to be transformed is

$$a(x) = \exp\left[\frac{i\theta\pi}{180}\right], \quad (2)$$

where  $\theta$  varies between 0 and  $360^\circ$ . The azimuth series was normalised to zero mean, e.g.  $a'(x) = a(x) - \bar{a}$ , prior to transformation. The resultant series of complex numbers was transformed to generate

$$W_x^{a'}(s) = \sum_{a'=0}^{N-1} a'(x)\psi\left[\frac{x' - x}{s}\right]. \quad (3)$$

The mother wavelet  $\psi$  is scaled by  $s$  and translated along the time series by  $x'$  for  $N$  data points. In the examples shown in this paper the mother wavelet is a real valued 6<sup>th</sup> order derivative of a Gaussian (DOG), with  $\delta_j = 0.1$  (see Torrence et al. 1998;  $m = 6$ ).  $W_x^{a'}(s)$  is the transformed version of the complex azimuth time series as a function of scale,  $s$ . Power of the complex time series is  $|W_x^{a'} + \bar{a}|^2$ . Scales are converted to Fourier periods using the methodology described by Torrence et al. (1998).

Real valued azimuths (in degrees) as a function of distance and wavenumber can then be calculated as  $\theta(x, k) = \zeta 180/\pi \bmod 360$ , where  $\bmod$  is the modulus operator, and  $\zeta$  is the argument of the transformed (complex) time series (Equation 3), and is computed as

$$\zeta = \tan^{-1}\left[\frac{\Im\{W_x^{a'}(\theta, k) + \bar{a}\}}{\Re\{W_x^{a'}(\theta, k) + \bar{a}\}}\right]. \quad (4)$$

Note that the mean of the complex time series,  $\bar{a}$ , is added to the reconstructed complex time series in this step. The inverse wavelet transformation is simply the sum of the signal in distance-wavenumber space over scales,  $j = 0, 1, \dots, J$ . Following Torrence et al. (1998)’s notation, the inverse transformation of the complex time series is

$$a_x = \bar{a} + \frac{\delta_j \delta t^{1/2}}{1.7379} \sum_{j=0}^J \frac{W_x^{a'}(s_j)}{s_j^{1/2}}, \quad (5)$$

for the DOG mother wavelet used in this study. Note subscript  $x$  denotes transformed time series. The denominator factor (here 1.7379) depends on the mother wavelet used in the transformation. Real valued bearings (in degrees) can be generated from  $a_x$

$$\theta_x = \tan^{-1}\left[\frac{\Im\{a_x\}}{\Re\{a_x\}}\right] \frac{180}{\pi} \bmod 360. \quad (6)$$

Filtered azimuth time series can now be generated by solving Equations 5 and 6 between scales of interest. Filtered river planforms can be estimated from these azimuths by forward geodetic transformation, which returns longitudes and latitudes given a starting position (e.g. the head of the river), bearings and distances. In this case, distances are scaled so that the final calculated position coincides with the actual river mouth. The WGS84 datum was used to perform the transformation. Whilst we consider only river paths in this study, it is straightforward to generalise this approach to other forms of path or directional data sequence (e.g. a time series of flow velocities and directions).

There are two main sources of uncertainty in the wavelet transformation described above. First, there is uncertainty in the position of mapped river planforms. The fidelity of mapped rivers was assessed by comparison with independent satellite imagery. At the scales of interest (i.e.  $> 2$  km) planforms are accurately reproduced away from flat topography and standing water (e.g. lakes). There is also an uncertainty,  $\delta\theta$  associated with measuring azimuths from discrete digital elevation data, which is inversely proportional to distance between cells,  $L$ , such that  $\sin(\delta\theta) = \delta x (\delta x^2 + L^2)^{-1/2}$  for simple east-west Euclidean flow paths, which yields an uncertainty of  $\delta\theta \sim 0.9^\circ$  for ASTER data ( $\delta x \approx 30$  m) if  $L = 2$  km. If  $L = 100$  km,  $\delta\theta \sim 0.02^\circ$ . Second, spectral leakage can generate uncertainties in calculated azimuths. A guide to the fidelity of the wavelet transform is the accuracy of reconstituted time series (i.e. generated by inverse transformation), which, for the examples in this paper, match the  $\theta(x)$  time series within a few percent in terms of error of the mean (Figure S1a-b of this document).

An alternative intuitive methodology is to transform eastings and northings generated from the azimuthal time series. As expected this approach gives the same results as transforming the complex form of the signal (Figure S1c-g of this document). Eastings and northings are calculated such that

$$e(x) = \sin(\pi\theta(x)/180), \quad n(x) = \cos(\pi\theta(x)/180), \quad (7)$$

where  $e(x)$  and  $n(x)$  vary between  $-1$  and  $1$ ,  $\theta$  is in degrees. The easting and northing distance-amplitude time series are then independently transformed into the distance-wavenumber domain. The time series were normalised to zero mean, e.g.  $e'(x) = e(x) - \bar{e}$ , prior to transformation. These real valued time series are converted using a continuous wavelet transformation and real valued mother wavelets. The two time series,  $e'(x)$  or  $n'(x)$ , are transformed such that,

$$W_x^e(s) = \sum_{x'=0}^{N-1} e'_x \psi \left[ \frac{x' - x}{s} \right], \quad \text{and} \quad W_x^n(s) = \sum_{x'=0}^{N-1} n'_x \psi \left[ \frac{x' - x}{s} \right], \quad (8)$$

where  $W_x^e(s)$  and  $W_x^n(s)$  are the transformed versions of the easting and northing time series as a function of scale,  $s$ . The easting and northing distance-amplitude time series can be reconstructed by summing their respective wavelet transforms across scales (i.e. the inverse transformation). Following Torrence and Compo's notation,

$$e_x = \frac{\delta_j \delta t^{1/2}}{1.7379} \sum_{j=0}^J \frac{W_x^e(s_j)}{s_j^{1/2}}, \quad \text{and} \quad n_x = \frac{\delta_j \delta t^{1/2}}{1.7379} \sum_{j=0}^J \frac{W_x^n(s_j)}{s_j^{1/2}}, \quad (9)$$

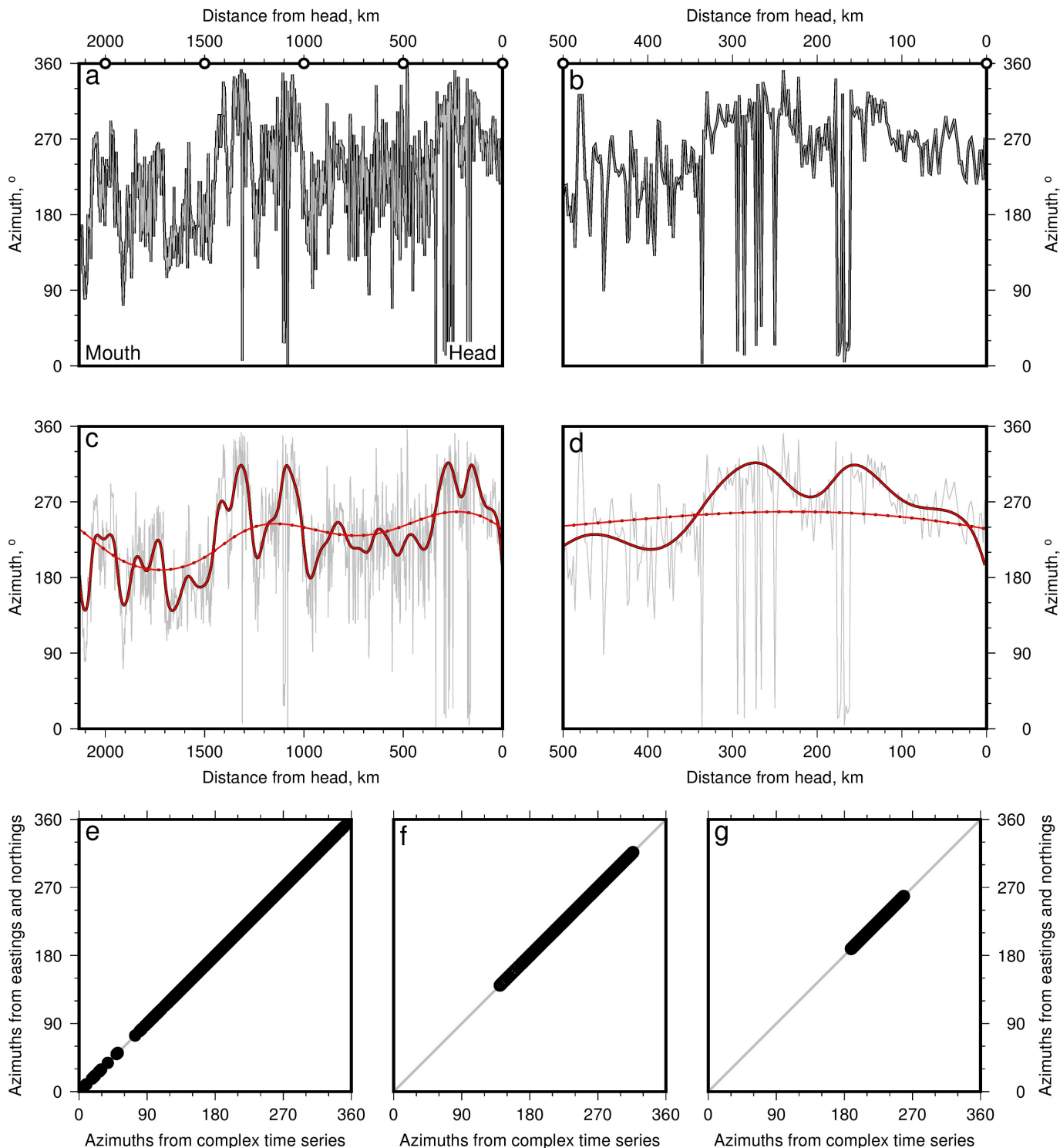
for the DOG mother wavelet used in this study. At this stage the means (e.g.  $\bar{e}$  and  $\bar{n}$ ) are added to the reconstructed time series. The azimuth time series as a function of distance can then be constructed using

$$\theta_x = \frac{180}{\pi} \arctan2(e_x + \bar{e}, n_x + \bar{n}). \quad (10)$$

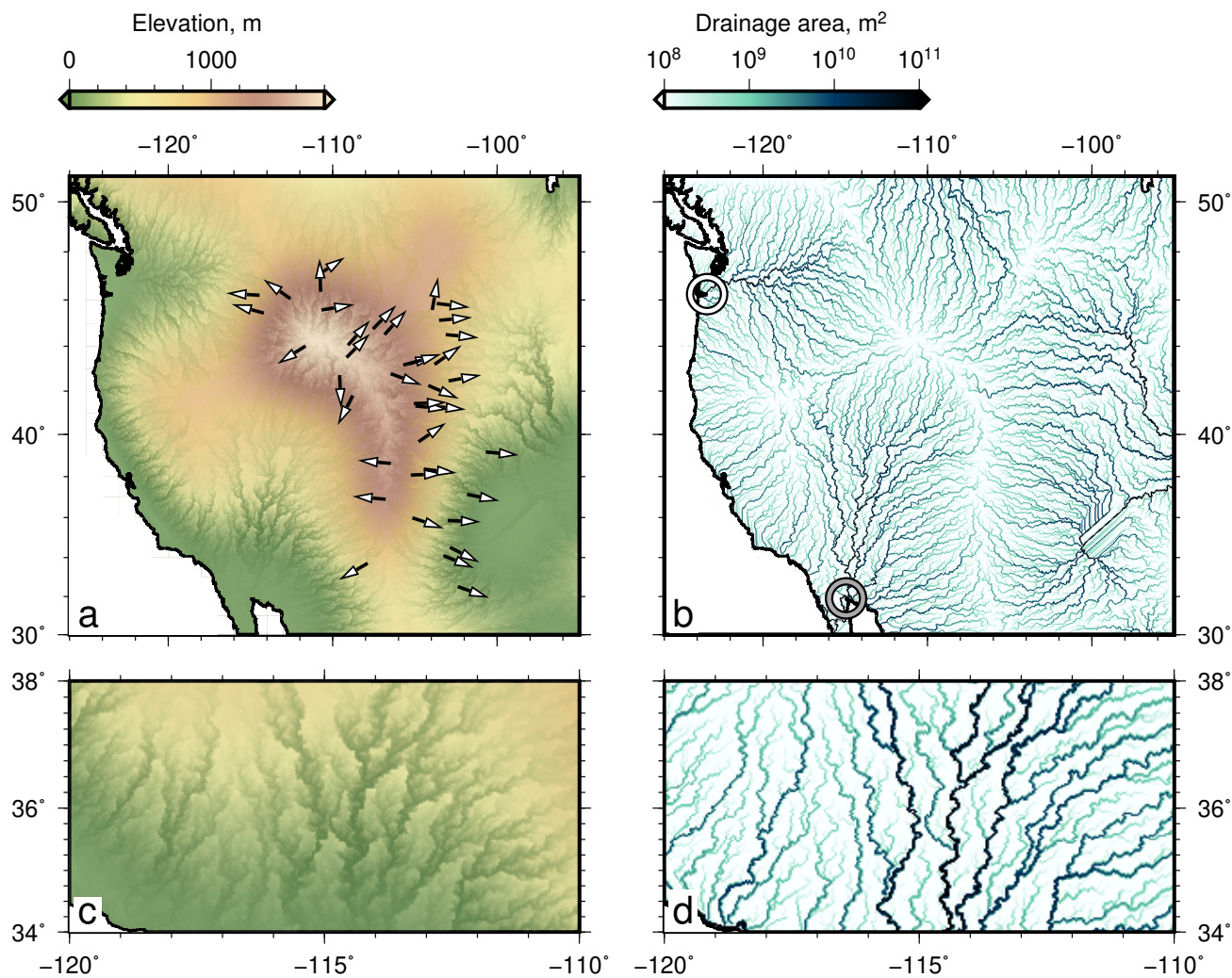
Filtering of the azimuth time series is performed by solving Equation 9 between scales of interest and calculating  $\theta_x$  using filtered eastings and northings (Equation 10).

### *Synthetic landscapes*

An example of a synthetic landscape is shown in Figure S2 of this document. This model was parameterised in exactly the same way as the one in the main paper apart from two changes (Figure 4). First, the modern coastline was inserted. Second, a different random uniform distribution of ( $\pm 50$  m) noise was used. Whilst the planform at small scales is clearly affected by these changes (e.g. the positions of meanders; cf. panel d and Figure 4d in main manuscript), large scale structure is essentially unchanged.



Supplementary Figure 1: **Wavelet transform of Colorado river flow directions.** (a) Black curve = azimuths of full resolution data set ( $\delta x = 2$  km). Gray = results from inverse wavelet transform. Circles atop panel are locations along Colorado river shown in Figure 2c of main manuscript. Panel (b) shows first 500 km in more detail. (c) & (d) Gray = full resolution azimuths. Black dotted and dash curves = azimuths filtered to remove wavelengths less than 100 km and 1000 km using complex time series. Red curves = results from transforming easting and northing time series. (e), (f) & (g) show azimuths calculated from the complex time series compared to those generated from easting and northing time series for full resolution,  $\lambda > 100$  km, and  $\lambda > 1000$  km, respectively. Gray line = 1:1 relationship.



Supplementary Figure 2: **Synthetic landscape.** (a)-(d) Model is setup in the same way as for Figure 4 in the main manuscript with the addition of the coastline and a different random noise distribution. See Figure 4 of main manuscript for annotations.